Precision Engineering 37 (2013) 117–128

Contents lists available at SciVerse ScienceDirect

Precision Engineering

journal homepage: www.elsevier.com/locate/precision

Kinematic modeling and calibration of a flexure based hexapod nanopositioner

Hongliang Shi [a], Hai-Jun Su [a,*], Nicholas Dagalakis [b], John A. Kramar [c]

[a] Department of Mechanical and Aerospace Engineering, The Ohio State University, Columbus, OH 43210, USA
[b] Engineering Laboratory, National Institute of Standards and Technology, USA
[c] Physical Measurement Laboratory, National Institute of Standards and Technology, USA

ARTICLE INFO

Article history:
Received 19 January 2012
Received in revised form 28 May 2012
Accepted 13 July 2012
Available online 21 July 2012

Keywords:
Nanopositioner
Flexure mechanisms
Hexapod platform
Calibration
Kinematics

ABSTRACT

This paper covers the kinematic modeling of a flexure-based, hexapod nanopositioner and a new method of calibration for this type of nanopositioner. This six degrees of freedom tri-stage nanopositioner can generate small displacement, high-resolution motions with high accuracy by actuating three inexpensive, high quality planar stages. Each stage is equipped with linear actuators. In this paper, we discuss the calibration of the nanopositioner and methods to improve its accuracy. First, we derive the kinematic model of the nanopositioner that is a Stewart platform with spherical joints. Based on this kinematic model, we then calculate the actuation data for a set of commands for decoupled and coupled motions. We use an interferometer and an autocollimator to measure the actual displacement and rotation of the platform. Finally, we obtain the Jacobian matrix of the moving platform for the controller. Experiments showed that with the calibration-corrected parameters, the maximum error is approximately 0.002° in rotations and 3.3 μm in translation for a workspace of ± 0.2° and ±200 μm in *x*, *y* and *z* direction.

1. Introduction

Flexure or compliant mechanisms [1] composed of flexure hinges and leaf springs have the advantage of no backlash and ultrahigh precision. They have been widely used in precision nanopositioners or naomanipulators which play an important role in emerging nanotechnology [2]. Compliant parallel platform mechanisms combine the advantages of flexure mechanisms and parallel platforms, and have received particular attention from nanotechnologists [3–7]. However, modeling and controller design has been a challenging task due to their inherent structural complexity and difficulties in measuring the six-degree-of-freedom (6DOF) positioning accuracy.

Kinematic calibration is the mapping of the output movement relative to the input to the actuators by means of physical experiments. It is one of the key steps in the development of a controller. A lot of prior work by other researchers has been done regarding kinematic modeling and calibration of flexure mechanisms. Dagalakis et al. [8] derived the kinematic model of a parallel robot link crane. Chen and Hsu [9] derived the kinematic model of a tripod machine tool. Culpepper and Anderson [10] designed and calibrated a monolithic spatial compliant nano-manipulator. Chen and Culpepper [11] designed and calibrated a six-axis micro-scale nanopositioner. Varadarajan and Culpepper [12,13] conducted the calibration of a dual-purpose positioner-fixture, which has six degrees of freedom. Chao et al. [14] presented a novel method for kinematic calibration of a planar parallel flexure positioner. Yao et al. [15] derived and calibrated a kinematic model of a planar micropositioning stage. Dong and co-workers [16] derived and tested a parallel kinematic model for integrated multi-axis nanopositioning. However, there is relatively little prior work for calibrating a parallel platform flexure mechanism. Recently Brouwera et al. [17] designed and built a flexure based hexapod nanopositioner. They derived a stiffness-matrix-based kinematic model, however, no calibration was done on this device.

Interferometers and autocollimators are commonly used instruments for calibration in precision engineering. Yang et al. [18] proposed a multi-probe scanning method, guided by means of three laser interferometers and one autocollimator. This method can measure five degrees of freedom simultaneously. In order to measure the displacement of the platform, a new set of calibrations should be made. Based on the calibrations, a new model for the controller can be derived. Parker et al. [19] has done related work by demonstrating a calibration-based modeling method for a dual-axis inclinometer.

In this paper, we derive the kinematic model and calibrate the motion of a hexapod platform nanoposioner (shown in the Fig. 1). The hexapod nanopositioner was previously built by the National Institute of Standards and Technology (NIST). The nanopositioner is composed of three main parts: base stages, struts and top platform. Three *X*–*Y* micro-positioning base stages, which can generate motion in two orthogonal directions, are symmetrically positioned

* Corresponding author.
E-mail address: su.298@osu.edu (H.-J. Su).

0141-6359/$ – see front matter © 2012 Elsevier Inc. All rights reserved.
http://dx.doi.org/10.1016/j.precisioneng.2012.07.006

Nomenclature

$\hat{T}$	instantaneous motion twist representing motion of the top platform
$\hat{T}^k$	instantaneous motion twist of the top platform by the kinematic model
$\hat{T}^c$	instantaneous motion twist of the top platform by the calibrated model
$\hat{T}^e$	measured instantaneous motion twist of the top platform
${}^c\hat{T}$	instantaneous motion twist representing motion of the reflective cube
${}^c\hat{T}^k$	instantaneous motion twist of the reflective cube by the kinematic model
${}^c\hat{T}^c$	instantaneous motion twist of the reflective cube by the calibrated model
${}^c\hat{T}^e$	measured instantaneous motion of the reflective cube
$\hat{U}$	actuation of the six linear motors
θ	rotational displacement of the top platform
δ	translational displacement of the top platform
$[J^k]$	the 6 by 6 Jacobian matrix of the top platform by the kinematic model
$[J^c]$	the 6 by 6 Jacobian matrix of the top platform by the calibrated model
$[J^e]$	the 6 by 6 Jacobian matrix of the top platform by experiments
$[J_{\text{cube}}]$	the 6 by 6 calibrated Jacobian matrix of the reflective cube
$[Ad]$	a 6 by 6 adjoint transformation matrix
$[R]$	a 3 by 3 rotational matrix
$[I]$	the 3 by 3 Identity matrix

on the base plane. The moving plate of each base stage supports two struts, which are firmly attached to the plate on one end through flexure joints. The struts have flexures at both attachment points. The struts are firmly attached on the base plate and the moving platform and allow motion to take place through elastic deformation of their flexures thus eliminating backlash and stiction. The moving platform is the load carrying part of the device. By means

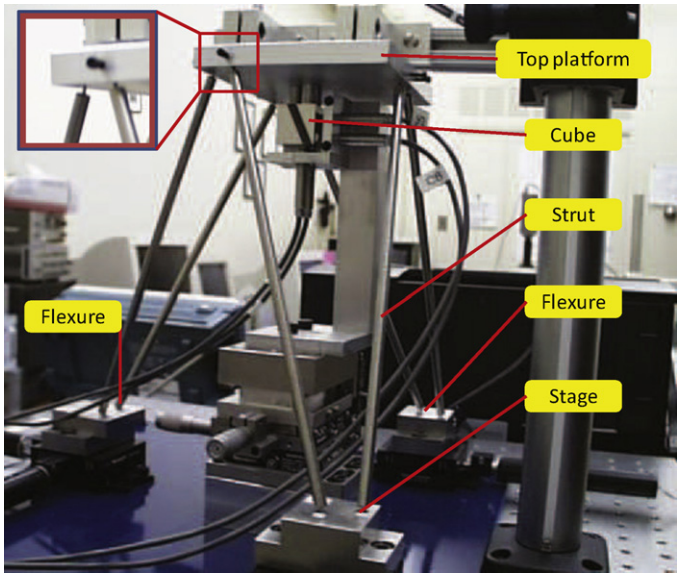

Fig. 1. The NIST hexapod nanopositioner.

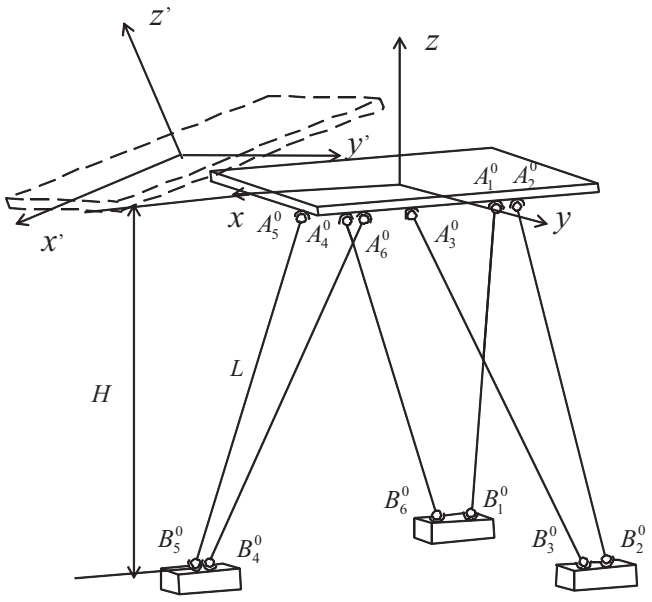

Fig. 2. The simplified kinematic model of the positioner.

of a kinematic model, we first derive the kinematic Jacobian matrix, which is used to generate suitable actuation samples for calibration. Using three interferometers and two autocollimators, we construct a calibration frame of reference for measuring the six degrees of freedom of the platform. Then, based on the experimental data, the calibrated Jacobian matrix is derived.

The rest of the paper is organized as follows. Section 2 derives the Jacobian matrix by kinematic modeling. Section 3 shows the calibration hardware set up, including the interferometers which measure the translational motions and the autocollimators which measure the rotational motions. In Section 4, we derive the Jacobian matrix of the cube and Jacobian matrix of the top platform by means of the kinematic model derived in Section 2 and the experimental measurements described in Section 3. Finally, in Section 5, the same 54 sets of actuation are applied to the kinematic model, calibrated model and the experimental device. Errors of the kinematic model and calibrated model are then calculated and analyzed.

2. Kinematic modeling

As shown in the Fig. 2, we place the global coordinate system at the home position of the geometrical center of the top platform. In the kinematic model, the short flexure joints of the struts are treated as spherical joints with three degrees of freedom, the centers of which are located at physical endpoints of the flexures, both at the base end and at the top platform end.

For convenience, we define the following parameters for describing the geometry of the kinematic model. For the base stages, the distance between the neighboring intersecting points of the struts is c_1. The distance between the non-neighbor intersecting points of the struts at the base platform is c_2. The struts have a total length L and diameter D, and have a short flexure joint of length l and diameter d at the both ends($L \gg l$). At the other ends of the six struts, the top square moving platform is rigidly attached through an additional flexure on each strut. The moving platform of thickness t carries the load of the device. The distance between the neighboring intersecting points of the struts at the top platform is c_3. The distance between the

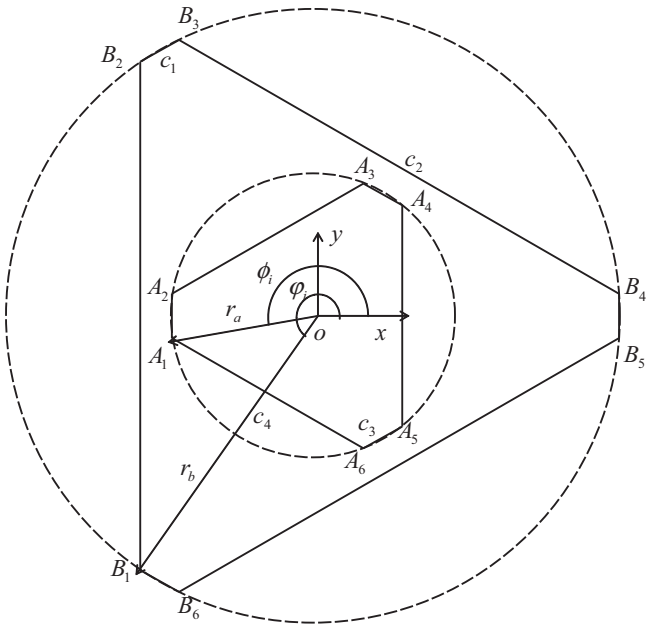

Fig. 3. Geometrical description of the top platform and bottom stage.

non-neighbor intersecting points of the struts at the top platform is c_4. See Fig. 3.

2.1. Geometry of the positioner

Fig. 3 shows the geometrical relationship of the 12 points. We denote the position of six points at the top platform and the base stages by $\mathbf{A}_i (i = 1, \ldots, 6)$ and by $\mathbf{B}_i (i = 1, \ldots, 6)$ respectively. The points on the moving platform can be described in the global coordinates as

$$\mathbf{A}_i^0 = [Z(\phi_i)] \begin{Bmatrix} r_a \\ 0 \\ -t/2 \end{Bmatrix}, \quad \mathbf{B}_i^0 = [Z(\psi_i)] \begin{Bmatrix} r_b \\ 0 \\ -H \end{Bmatrix}, \tag{1}$$

where $[Z(\cdot)]$ is the 3 by 3 rotation matrix about the z axis. r_A and r_B are the radii of the strut attachment points (bottom plates in home position). Angles ϕ_i and ψ_i are tabulated in Table 1.

2.2. Positional and velocity constraint equations

By the kinematic model shown Fig. 2, the kinematic constraint equation of this platform is

$$(\mathbf{A}_i - \mathbf{B}_i)^T (\mathbf{A}_i - \mathbf{B}_i) - L^2 = 0, \tag{2}$$

where L is the strut length.

The instantaneous small motion of the platform at the original position is obtained by taking the derivative of the kinematic Eq. (2) with respect to time and substituting with geometric parameters, written as

$$(\mathbf{A}_i^0 - \mathbf{B}_i^0)^T (\omega \times \mathbf{A}_i^0 + \mathbf{v}) = (\mathbf{A}_i^0 - \mathbf{B}_i^0)^T \delta \mathbf{B}_i \quad i = 1, \ldots, 6. \tag{3}$$

Table 1
Geometric dimensions of the hexapod nanopositioner.

r_a = 81.44 mm, r_b = 138.92 mm, t = 13.2 mm, H = 221.93 mm, L = 240 mm
c_1=20 mm, c_2=230 mm, c_3=20 mm, c_4=100 mm
$\phi_1 = 189°$, $\phi_2 = 171°$, $\phi_3 = 69°$, $\phi_4 = 51°$, $\phi_5 = -51°$, $\phi_6 = -69°$
$\psi_1 = 236°$, $\psi_2 = 124°$, $\psi_3 = 116°$, $\psi_4 = 4°$, $\psi_5 = -4°$, $\psi_6 = -116°$

Here $\delta \mathbf{B}_i$ is the instantaneous movement of points $\mathbf{B}_i$, written as:

$$\delta \mathbf{B}_{1,6} = \begin{Bmatrix} U_{1x} \\ U_{1y} \\ 0 \end{Bmatrix}, \quad \delta \mathbf{B}_{2,3} = \begin{Bmatrix} U_{2x} \\ U_{2y} \\ 0 \end{Bmatrix}, \quad \delta \mathbf{B}_{4,5} = \begin{Bmatrix} U_{3x} \\ U_{3y} \\ 0 \end{Bmatrix} \tag{4}$$

where U_{jx}, $U_{jy} (j = 1, 2, 3)$ represent the horizontal displacement of the three stages on the base, i.e., the six input actuation data. In small deflection, the $\mathbf{v}$ and ω in Eq. (3) are the instantaneous linear velocity and angular velocity of the top platform, written as:

$$\omega = \begin{Bmatrix} \theta_x \\ \theta_y \\ \theta_z \end{Bmatrix}, \quad \mathbf{v} = \begin{Bmatrix} \delta_x \\ \delta_y \\ \delta_z. \end{Bmatrix} \tag{5}$$

2.3. Derivation of the Jacobian matrix

Now we can write Eq. (3) in matrix form as

$$[J_l]\hat{T} = [J_r]\hat{U}, \tag{6}$$

where $\hat{T} = (\theta_x, \theta_y, \theta_z, \delta_x, \delta_y, \delta_z)^T$ is the motion twist of the top platform and $\hat{U} = (U_{1x}, U_{2x}, U_{2y}, U_{3x}, U_{3y}, U_{1y})^T$ is the actuating displacement of the linear motors. The left matrix $[J_l]$ has the following form

$$[J_l] = \begin{Bmatrix} (\mathbf{A}_1^0 - \mathbf{B}_1^0)^T [-\mathbf{A}_1^0 \times \ | \ \mathbf{I}] \\ \vdots \\ (\mathbf{A}_6^0 - \mathbf{B}_6^0)^T [-\mathbf{A}_6^0 \times \ | \ \mathbf{I}] \end{Bmatrix}, \tag{7}$$

where $\mathbf{I}$ is the 3 by 3 identity matrix and symbol $[\mathbf{a} \times]$ represents the cross product matrix defined as

$$[\mathbf{A}_i^o \times] = \begin{bmatrix} 0 & A_{iz}^0 & -A_{iy}^0 \\ -A_{iz}^0 & 0 & A_{ix}^0 \\ A_{iy}^0 & -A_{ix}^0 & 0 \end{bmatrix}, \quad \forall \mathbf{a} = (a_x, \ a_y, \ a_z)^T. \tag{8}$$

The right matrix $[J_r]$ has the following form

$$\begin{bmatrix} A_{1x}^0 - B_{1x}^0 & 0 & 0 & 0 & 0 & A_{1y}^0 - B_{1y}^0 \\ 0 & A_{2x}^0 - B_{2x}^0 & A_{2y}^0 - B_{2y}^0 & 0 & 0 & 0 \\ 0 & A_{3x}^0 - B_{3x}^0 & A_{3y}^0 - B_{3y}^0 & 0 & 0 & 0 \\ 0 & 0 & 0 & A_{4y}^0 - B_{4y}^0 & A_{4x}^0 - B_{4x}^0 & 0 \\ 0 & 0 & 0 & A_{5y}^0 - B_{5y}^0 & A_{5x}^0 - B_{5x}^0 & 0 \\ A_{6x}^0 - B_{6x}^0 & 0 & 0 & 0 & 0 & A_{6y}^0 - B_{6y}^0 \end{bmatrix}. \tag{9}$$

It follows that the Jacobian matrix relating the motion twist $\hat{T}$ to the six actuator inputs $\hat{U}$ is calculated from Eq. (6)

$$[J^k] = [J_l]^{-1}[J_r] =$$

$$\begin{bmatrix} -0.0016 & 0.0016 & 0.0009 & -0.0019 & 0.0000 & -0.0009 \\ -0.0009 & -0.001 & 0.0016 & 0.0000 & -0.0019 & 0.0016 \\ 0.0018 & -0.0018 & 0.0010 & -0.0020 & 0.0000 & -0.0010 \\ 0.2431 & 0.2431 & 0.1563 & 0.0000 & -0.5138 & 0.1563 \\ 0.1563 & -0.1563 & -0.4236 & -0.1529 & 0.0000 & 0.4236 \\ 0.0760 & 0.0760 & 0.1316 & 0.0000 & 0.1519 & 0.1316 \end{bmatrix}, \tag{10}$$

where we have substituted the geometric parameters in Table 1.

3. Calibration hardware set up

In this section, we describe the setup of the physical measurement and the calibration process. To accurately measure the movement of the platform, a high precision reflective cube is

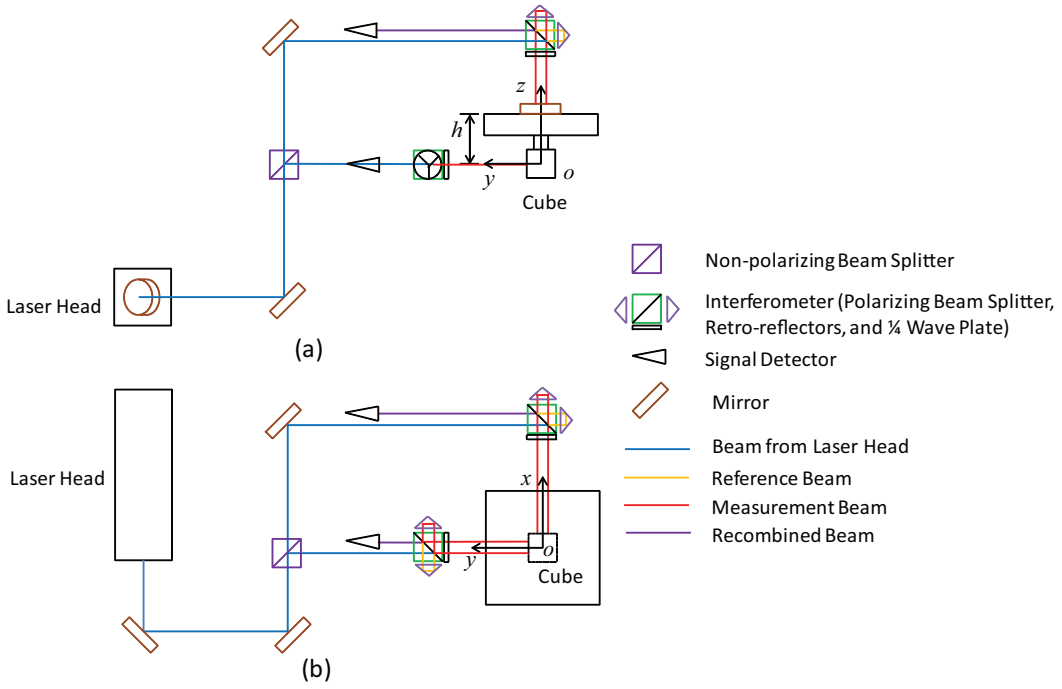

Fig. 4. Interferometer set up for measuring translational displacements; (a) schematic front view; (b) schematic top view. For better clarity, X and Z interferometers are not shown in (a) and (b), respectively.

attached to the lower side of the top moving platform and translates and rotates with the top platform as a single rigid body (See Fig. 1). The cube has five highly polished reflecting sides orthogonal to each other within 1.4E−3°. The center of the cube and center of the top platform are both aligned along the z axis in the local coordinate frame.

The calibration process is divided into two major steps. The first step is to measure the translational motions of the cube with interferometers. The second step is to measure the rotational motion of the cube with an autocollimator. We describe each in the following subsections. In both steps, the same set of calibration actuator position commands is fed to the computer controller and the output movements of the cube are recorded (translation or rotation).

3.1. Measuring Translational Displacement

Our first step is to measure the three-axis translational motion of the cube using interferometers. The physical set up is shown in Fig. 4. We use a Hewlett-Packard hp5507A Laser Position Transducer system[1]. An interferometer is an optical calibration instrument that makes use of the interference of light that has traversed different pathways to measure the difference in distance traversed. Typically one path (the reference beam) is fixed, and the other path (the measurement beam) is reflected off of a moving mirror. As the mirror moves along to the measurement beam path, the beam path length increases (or decreases), and the reflected beam, superimposed on the reference beam, interferes alternately constructively and destructively as the beam path changes by single wavelengths. These bright and dark interference fringes are captured by signal detectors and fed into the interferometer

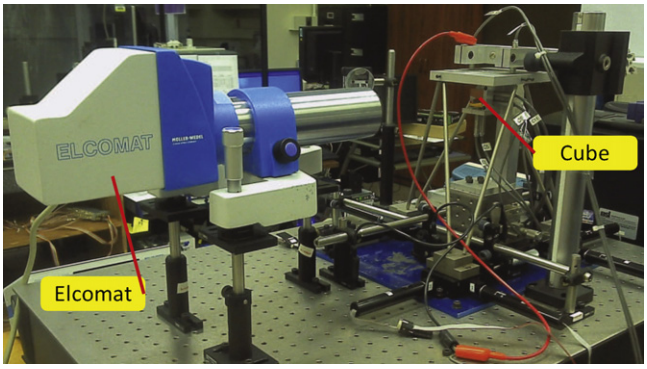

Fig. 5. Elcomat setting for measuring rotational displacements about *x* and *z* axes. Rotate the autocollimator to measure the rotational displacement about *y* axis.

control unit to interpolate between fringes and to integrate the number of fringes traversed. The fringe detection and interpolation can also be accomplished using a heterodyne method, as in our case, in which the Doppler shift caused by the moving mirror is measured as a change in the difference frequency between the reference and measurement beams, and is integrated to yield displacement.

In our set up, the interferometer laser head sends one laser beam that is split into three beams, directed by mirrors to the interferometer beam splitters. Two of the interferometers are aimed at the precision cube along the *x* and *y* axis. The resulting signals are used to measure translational motion along *x* and *y*, denoted by ${}^{c}\delta_{x}^{e}$ and ${}^{c}\delta_{y}^{e}$. The third interferometer is aligned with a mirror that is fixed at the center of the top platform surface. We measure the translational motion ${}^{c}\delta_{z}^{e}$ along the *z* axis using this third beam. Alignment of the interferometer beams with the mirror surfaces is done to better than 2E−5° by checking the overlap of the reflections with the source.

The stage is driven through a set of 54 calibration positions. The motions and measurements are quasi-static. At each position,

[1] Certain commercial equipment, instruments, or materials are identified in this paper in order to specify the experimental procedure adequately. Such identification is not intended to imply recommendation or endorsement by the National Institute of Standards and Technology, nor is it intended to imply that the materials or equipment identified are necessarily the best available for the purpose.

Table 2
Commanded motion of the platform $\hat{T}_i^k$ and the measured motion of the cube ${}^c\hat{T}_i^e$ from experimental measurements.

	θ_x (°)	θ_y (°)	θ_z (°)	δ_x (μm)	δ_y (μm)	δ_z (μm)
$\hat{T}_1^k$	0.1	0	0	0	0	0
${}^c\hat{T}_1^e$	9.72E−02	2.21E−04	−4.38E−04	2.31E+00	4.58E+01	2.83E+00
$\hat{T}_2^k$	0	0.1	0	0	0	0
${}^c\hat{T}_2^e$	−1.43E−03	9.50E−02	−1.94E−03	−5.83E+01	5.58E+00	−2.42E+00
$\hat{T}_3^k$	0	0	0.1	0	0	0
${}^c\hat{T}_3^e$	2.20E−03	1.83E−03	9.97E−02	−2.62E+00	9.27E+00	−1.69E+00
$\hat{T}_4^k$	0	0	0	100	0	0
${}^c\hat{T}_4^e$	−1.75E−06	1.94E−04	9.51E−04	9.91E+01	−2.21E+00	−6.18E−01
$\hat{T}_5^k$	0	0	0	0	100	0
${}^c\hat{T}_5^e$	−6.44E−05	8.25E−05	5.83E−05	3.74E+00	9.88E+01	5.78E−01
$\hat{T}_6^k$	0	0	0	0	0	100
${}^c\hat{T}_6^e$	3.56E−04	1.13E−03	1.28E−03	4.92E+00	3.38E−01	9.59E+01

40 interferometer or autocollimator readings are averaged, taking approximately 30 s. The calibration position sequence includes several returns to the nanopositioner home position to check repeatability and drift.

3.2. Measuring rotational displacement

The second step is to measure the rotational motion of the cube by using an electronic autocollimator (Elcomat 3000)[1]. An autocollimator is an optical measurement instrument for measuring small angular deviations of inclination in two orthogonal axes. A slight alteration of the angle between the optical axis of the autocollimator and the mirror causes a deviation which can be determined precisely. According to the manufacturer, the measurement accuracy of the Elcomat 3000 is $\pm 7 \times 10^{-5}$ °, with a measuring range of 0.55 °.

Fig. 5 shows the hardware set up for measuring the rotation about the x and z axes. The autocollimator has to be moved to point at the other cube face to measure the rotation about the y axis. By feeding the calibration set of position commands to the actuators, we record the output rotational movement of the cube over a representative range of motion, denoted by ${}^c\theta_x^e$, ${}^c\theta_y^e$, ${}^c\theta_z^e$. The same set of 54 calibration positions are used as previously. All measurement sets are referenced to their initial measurement of the home position of the nanopositioner stage.

4. Data collection and processing

In this section, we derive the calibrated Jacobian matrix of the top platform by means of the kinematic Jacobian matrix from Section 2 and the experimental data acquired in Section 3. We first derive the calibrated Jacobian matrix of the cube center. Coordinate translation is then used to obtain the calibrated Jacobian matrix of the top platform.

4.1. Jacobian matrix of the cube center

By using Eq. (10), we first calculate the actuation $\hat{U}_i^k$ to command the platform to move only in single degree of freedom, $\hat{T}_i^k$ as shown in the Table 2. That is,

$$\hat{U}_i^k = [J^k]^{-1}\hat{T}_i^k, \quad i = 1, \ldots, 6. \tag{11}$$

Then we measure the displacement (rotation and translation) of the cube center with the interferometer and the autocollimator, denoted by

$${}^c\hat{T}_i^e = \begin{bmatrix} {}^c\theta_{ix}^e & {}^c\theta_{iy}^e & {}^c\theta_{iz}^e & {}^c\delta_{ix}^e & {}^c\delta_{iy}^e & {}^c\delta_{iz}^e \end{bmatrix}^T, \quad i = 1, \ldots, 6, \tag{12}$$

which are tabulated in Table 2. Lastly, the Jacobian matrix relating the displacement of the cube to the actuator inputs is calculated as

$$[J_{\text{cube}}] = \begin{bmatrix} {}^c\hat{T}_1^e & {}^c\hat{T}_2^e & {}^c\hat{T}_3^e & {}^c\hat{T}_4^e & {}^c\hat{T}_5^e & {}^c\hat{T}_6^e \end{bmatrix} \begin{bmatrix} \hat{U}_1^k & \hat{U}_2^k & \hat{U}_3^k & \hat{U}_4^k & \hat{U}_5^k & \hat{U}_6^k \end{bmatrix}^{-1}. \tag{13}$$

By substituting ${}^c\hat{T}_i^e$ from Table 2 and $\hat{U}_i^k$ calculated in Eq. (11), we obtain the numerical $[J_{\text{cube}}]$ as

$$\begin{bmatrix} -0.00151 & 0.00155 & 0.00092 & -0.00185 & 0.00004 & -0.00095 \\ -0.00083 & -0.00089 & 0.00158 & -0.00004 & -0.00176 & 0.00155 \\ 0.00185 & -0.00170 & 0.00103 & -0.00203 & -0.00002 & -0.00099 \\ 0.27679 & 0.27470 & 0.09127 & -0.00512 & -0.43932 & 0.12351 \\ 0.11332 & -0.12952 & -0.38636 & -0.21076 & 0.00592 & 0.39065 \\ 0.06922 & 0.07608 & 0.12106 & -0.00192 & 0.15147 & 0.12492 \end{bmatrix}. \tag{14}$$

4.2. Jacobian matrix of the top platform

Note that the cube is assembled directly below the top platform. Therefore the transformation is a pure translation along the z axis by a height h, represented by a vector $\mathbf{t} = (0, 0, \mathbf{h})^T$. To obtain the calibrated Jacobian matrix of top platform $[J^c]$, we just need to apply a pure translational transformation to $[J_{\text{cube}}]$, calculated as

$$[J^c] = [Ad][J_{\text{cube}}] = \begin{bmatrix} -0.0015 & 0.0016 & 0.0009 & -0.0018 & 0.0000 & -0.0010 \\ -0.0008 & -0.0009 & 0.0016 & 0.0000 & -0.0018 & 0.0016 \\ 0.0018 & -0.0017 & 0.0010 & -0.0020 & -0.0000 & -0.0010 \\ 0.2506 & 0.2465 & 0.1411 & -0.0065 & -0.4948 & 0.1724 \\ 0.1611 & -0.1784 & -0.4153 & -0.1522 & 0.0048 & 0.4206 \\ 0.0692 & 0.0761 & 0.1211 & -0.0019 & 0.1515 & 0.1249 \end{bmatrix}, \tag{15}$$

where $[Ad]$ is the well known adjoint matrix for coordinate transformation of Jacobian matrices [20], written as

$$[Ad] = \begin{bmatrix} \mathbf{I} & \mathbf{0} \\ [\mathbf{t}\times] & \mathbf{I} \end{bmatrix} = \begin{bmatrix} 1 & 0 & 0 & 0 & 0 & 0 \\ 0 & 1 & 0 & 0 & 0 & 0 \\ 0 & 0 & 1 & 0 & 0 & 0 \\ 0 & h & 0 & 1 & 0 & 0 \\ -h & 0 & 0 & 0 & 1 & 0 \\ 0 & 0 & 0 & 0 & 0 & 1 \end{bmatrix}, \tag{16}$$

where $h = 31.57$ mm.

5. Error calculation and error analysis

In this section, we will calculate and analyze the errors of the kinematic model and the calibrated model.

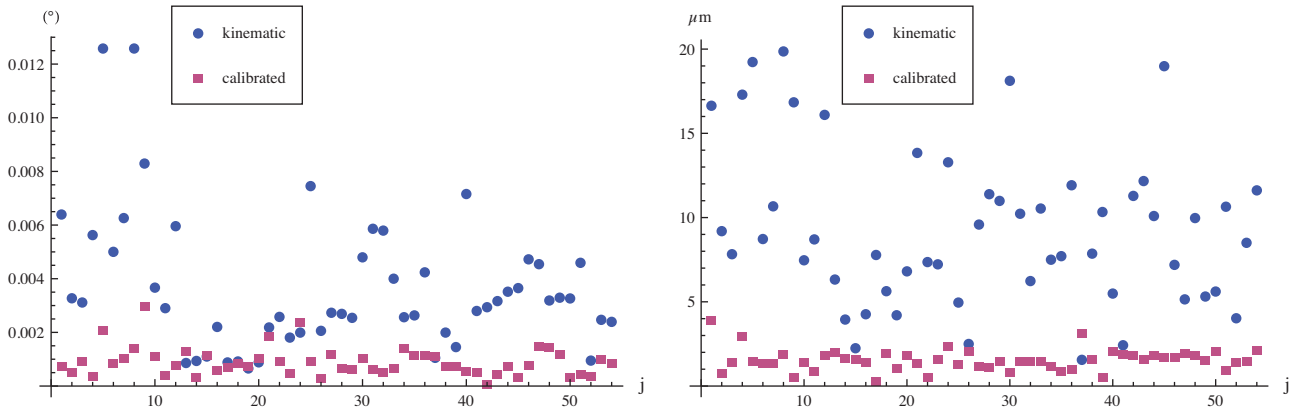

Fig. 6. Comparison of the kinematic model and the calibrated model. The left figure plots the norm of rotational error $\|\Delta\theta_j\|$. And the right figure plots the norm of translational error $\|\Delta\delta_j\|$. The dotted markers represent the kinematic model and the square markers represent the calibrated model.

5.1. Calculate model errors

Now we calculate the errors of the kinematic model and the calibrated model and compare them with the experimental measurements using the following steps.

1 Choose 54 sets of translation and rotation measurements of the top platform, which consists of 24 sets of single degree of freedom motions and 30 sets of coupled motions, denoted by

$$\hat{T}_j^c = (\theta_{jx}^c, \theta_{jy}^c, \theta_{jz}^c, \delta_{jx}^c, \delta_{jy}^c, \delta_{jz}^c)^T, \quad (j = 1, \ldots, 54).$$

2 Calculate the actuation required to achieve the commanded motion $\hat{T}_j^c$ by

$$\hat{U}_j = \hat{T}_j^c [J^c]^{-1} = \begin{bmatrix} \theta_{jx}^k & \theta_{jy}^k & \theta_{jz}^k & \delta_{jx}^k & \delta_{jy}^k & \delta_{jz}^k \end{bmatrix}^T.$$

3 Calculate the motion predicted from the kinematic model by

$$\hat{T}_j^k = [J^k]\hat{U}_j.$$

4 Feed the actuation $\hat{U}_j$ to the controller and measure the motion of the top platform as

$$\hat{T}_j^e = \begin{bmatrix} \theta_{jx}^e & \theta_{jy}^e & \theta_{jz}^e & \delta_{jx}^e & \delta_{jy}^e & \delta_{jz}^e \end{bmatrix}^T.$$

5 Calculate the error of the kinematic model as

$$\Delta\hat{T}_j^k = \hat{T}_j^e - \hat{T}_j^k = \begin{Bmatrix} \Delta\theta_j^k \\ \Delta\delta_j^k \end{Bmatrix}, \quad (j = 1, \ldots, 54),$$

where $\Delta\theta_j^k = (\theta_{jx}^e - \theta_{jx}^k, \theta_{jy}^e - \theta_{jy}^k, \theta_{jz}^e - \theta_{jz}^k)^T$, $\Delta\delta_j^k = (\delta_{jx}^e - \delta_{jx}^k, \delta_{jy}^e - \delta_{jy}^k, \delta_{jz}^e - \delta_{jz}^k)^T$.

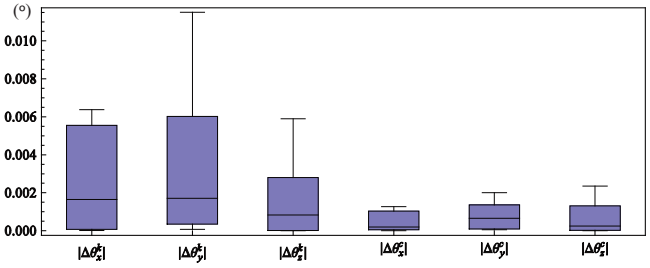

Fig. 7. Distribution plotting of $|\Delta\theta^k|$ and $|\Delta\theta^c|$.

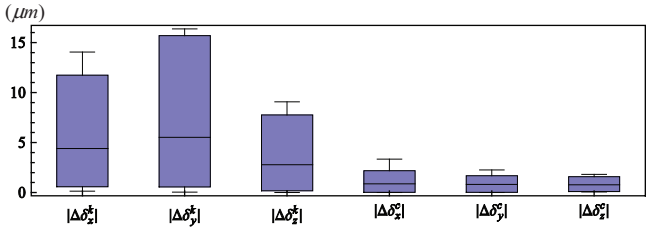

Fig. 8. Distribution plotting of $|\Delta\delta^k|$ and $|\Delta\delta^c|$.

6 Calculate the error of the calibrated model as

$$\Delta\hat{T}_j^c = \hat{T}_j^e - \hat{T}_j^c = \begin{Bmatrix} \Delta\theta_j^c \\ \Delta\delta_j^c \end{Bmatrix}, \quad (j = 1, \ldots, 54),$$

where $\Delta\theta_j^c = (\theta_{jx}^e - \theta_{jx}^c, \theta_{jy}^e - \theta_{jy}^c, \theta_{jz}^e - \theta_{jz}^c)^T$, $\Delta\delta_j^c = (\delta_{jx}^e - \delta_{jx}^c, \delta_{jy}^e - \delta_{jy}^c, \delta_{jz}^e - \delta_{jz}^c)^T$.

5.2. Error Analysis

To compare the errors of the kinematic model and the calibrated model, we plot the norm of rotational and translational errors in Fig. 6. It can be seen that the calibrated Jacobian matrix significantly improved the accuracy of kinematic Jacobian matrix by

Table 3
The range of the error of the calibrated model $\Delta\hat{T}_j^c$.

	$\Delta\theta_{jx}^c$(°)	$\Delta\theta_{jy}^c$(°)	$\Delta\theta_{jz}^c$(°)	$\Delta\delta_{jx}^c$ (μm)	$\Delta\delta_{jy}^c$ (μm)	$\Delta\delta_{jz}^c$ (μm)
Max	0.00127	0.00105	0.00235	3.34041	2.27184	0.11
Min	−0.00119	−0.002	−0.0009	−2.1961	−1.50408	−1.82
Standard deviation	0.000276979	0.000387935	0.00046507	0.686572	0.570813	0.410767

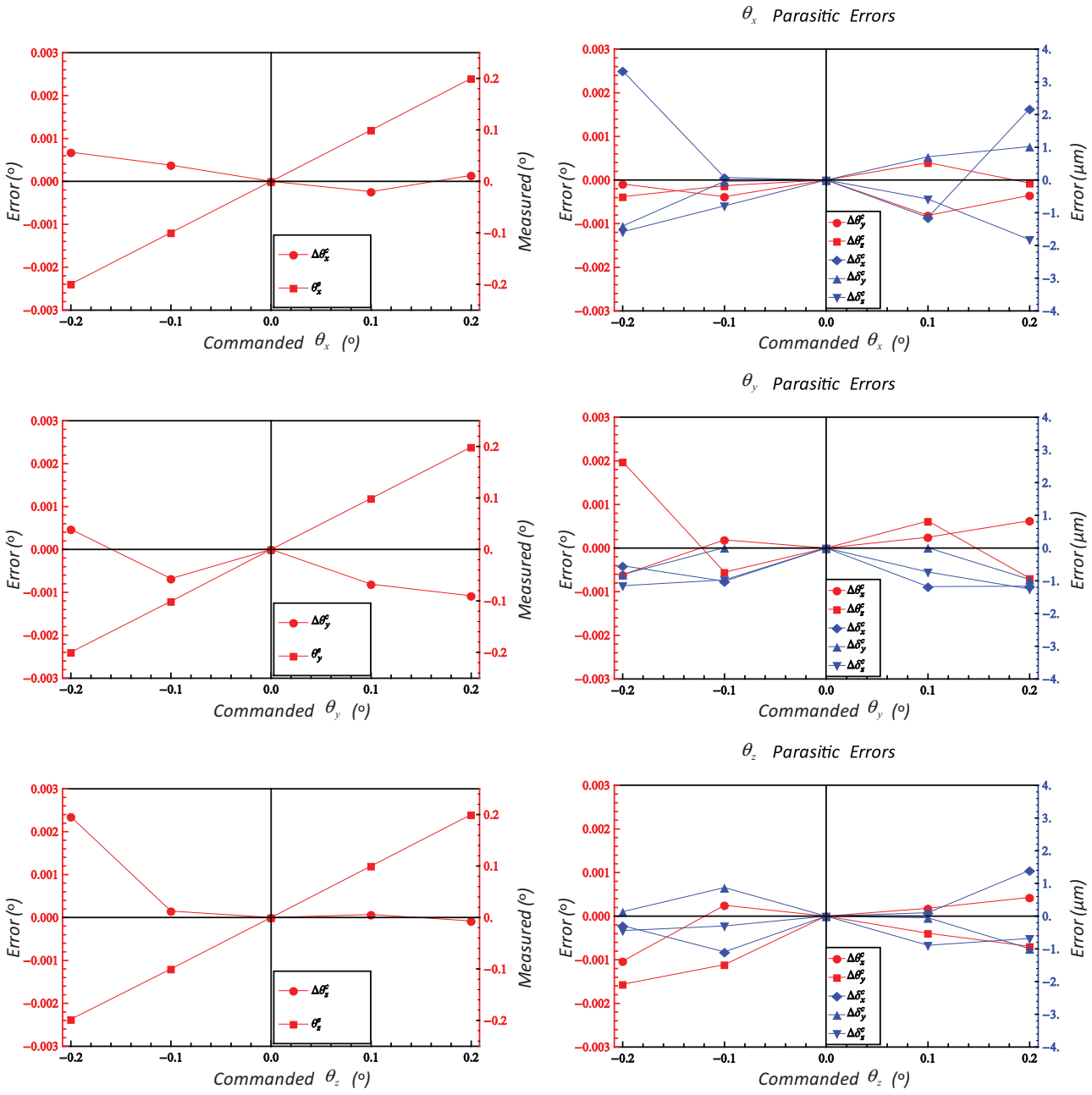

Fig. 9. Command rotational displacement vs. measured rotational displacement and parasitic error. (For interpretation of the references to color in the text, the reader is referred to the web version of the article.)

approximately four to five times. The details are described below. In terms of the rotational errors, the maximum and the mean of the kinematic model error $\Delta\theta_j^k$ are about 0.0126° and 0.0037° while those of the calibrated model $\Delta\theta_j^c$ are about 0.0030° and 0.0009°. With regard to the translational error, the maximum and the mean of $\Delta\delta_j^k$ are about 19.91 μm and 9.33 μm. After the calibration, these two errors are reduced to about 3.95 μm and 1.60 μm.

Now, we analyze the error of the calibrated Jacobian matrix J^c by means of $\Delta\hat{T}_j^c$. The Figs. 7 and 8 respectively shows the distribution of the absolute errors of kinematic and calibrated rotational and translational displacements about axis *x*, *y*, *z*. The box plotting contains the data with 90 % confidence. The maximum mean error for the calibrated model is $|\Delta\theta_y^c|$, around 0.001° and $|\Delta\delta_x^c|$, around 1 μm. Based on the distribution shown in Figs. 7 and 8, the standard deviation is calculated and shown in Table 3.

Table 3 shows the maximum and minimum values of the calibrated model compared with the experimental results. We conclude that the accuracy of the control is improved by means of the calibrated Jacobian [J^c]. The maximum error of the rotation is 0.0024° and the maximum standard deviation of the error of the rotation is 0.000465°. The maximum error of translation is 3.34 μm and the maximum standard deviation of the error of the translation is 0.686572 μm for a workspace of ± 200 μm by ± 200 μm by ± 200 μm by ± 0.2° by ± 0.2° by ±0.2°.

There are two lines in the left three plots of Fig. 9. One line shows the measured vs. commanded rotational displacements about axes

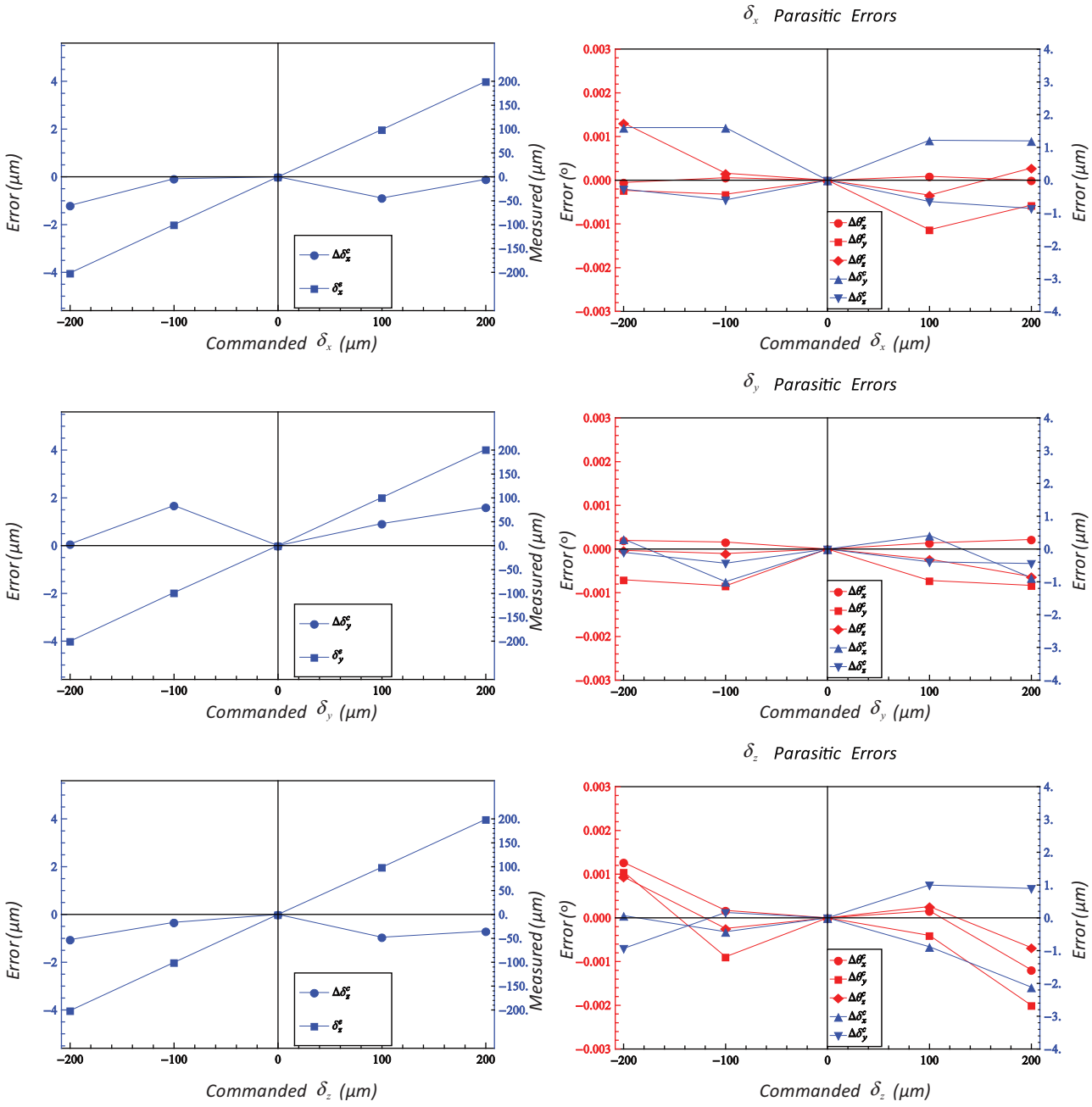

Fig. 10. Command translational displacement vs. measured translational displacement and parasitic error.

x, *y*, *z*. The other line shows the errors. The right three plots show the parasitic errors in the other five directions. Note that the red lines represent the errors of rotation and blue lines represent the errors of translation. The unit of the left red vertical axis is degree while the unit of the right blue vertical axis is μm. Similarly the measured vs. commanded translational displacements along axes *x*, *y*, *z* are plotted in the left column of Fig. 10 while the parasitic errors are plotted in the right column. As one can see, the measured displacements are linear with the commanded displacements as expected. The parasitic error is very low.

6. Conclusion

In conclusion, we have presented a two-phase platform calibration method for a hexapod nanopositioner. First, a kinematic model is derived for the nanopositioner platform. Next, a new calibration set for the platform is determined using an interferometer and an autocollimator to measure the displacements in six degrees of freedom. Kinematic-model-based calibration is used to get more accurate results. The results show that the maximum of rotational error is 0.0024° and the maximum of translational error is 3.34 μm. In future work, a controller would be developed based on the calibrated Jacobian matrix. Furthermore, this calibration method can be applied to a small-scale hexapod platform realized using microelectromechanical systems.

Appendix A.

Table 4.

Table 4
54 sets of displacement.

	θ_x (°)	θ_y (°)	θ_z (°)	δ_x (μm)	δ_y (μm)	δ_z (μm)
$j=1$; $\hat{T}_i^c$	1.00E−01	0.00E+00	0.00E+00	0.00E+00	0.00E+00	0.00E+00
$j=1$; $\hat{T}_i^k$	1.03E−01	−2.14E−04	5.07E−04	−2.66E+00	8.02E+00	−3.09E+00
$j=1$; $\hat{T}_i^e$	9.98E−02	−8.10E−04	4.00E−04	−1.15E+00	7.12E−01	−5.80E−01
	0.00E+00	1.00E−01	0.00E+00	0.00E+00	0.00E+00	0.00E+00
$j=2$	1.49E−03	1.05E−01	1.96E−03	6.45E+00	−6.68E+00	2.72E+00
	2.50E−04	9.92E−02	6.20E−04	−1.18E+00	1.22E−02	−7.30E−01
	0.00E+00	0.00E+00	1.00E−01	0.00E+00	0.00E+00	0.00E+00
$j=3$	−2.30E−03	−1.94E−03	1.00E−01	1.78E+00	−8.19E+00	1.85E+00
	1.80E−04	−3.90E−04	1.00E−01	1.05E−01	−4.92E−02	−8.90E−01
	0.00E+00	0.00E+00	0.00E+00	1.00E+02	0.00E+00	0.00E+00
$j=4$	2.02E−05	−1.96E−04	−9.73E−04	1.01E+02	2.35E+00	6.12E−01
	9.00E−05	−1.13E−03	−3.40E−04	9.91E+01	1.22E+00	−6.50E−01
	0.00E+00	0.00E+00	0.00E+00	0.00E+00	1.00E+02	0.00E+00
$j=5$	6.85E−05	−7.23E−05	−1.55E−05	−3.83E+00	1.01E+02	−6.38E−01
	1.40E−04	−7.20E−04	−2.30E−04	4.13E−01	1.01E+02	−3.90E−01
	0.00E+00	0.00E+00	0.00E+00	0.00E+00	0.00E+00	1.00E+02
$j=6$	−3.70E−04	−1.20E−03	−1.31E−03	−5.90E+00	−1.27E−01	1.04E+02
	1.60E−04	−4.00E−04	2.60E−04	−8.80E−01	1.00E+00	9.91E+01
	−1.00E−01	0.00E+00	0.00E+00	0.00E+00	0.00E+00	0.00E+00
$j=7$	−1.03E−01	2.14E−04	−5.07E−04	2.66E+00	−8.02E+00	3.09E+00
	−9.96E−02	−3.80E−04	−1.30E−04	8.06E−02	−3.93E−02	−7.90E−01
	0.00E+00	−1.00E−01	0.00E+00	0.00E+00	0.00E+00	0.00E+00
$j=8$	−1.49E−03	−1.05E−01	−1.96E−03	−6.45E+00	6.68E+00	−2.72E+00
	1.90E−04	−1.01E−01	−5.50E−04	−1.01E+00	1.53E−02	−9.70E−01
	0.00E+00	0.00E+00	−1.00E−01	0.00E+00	0.00E+00	0.00E+00
$j=9$	2.30E−03	1.94E−03	−1.00E−01	−1.78E+00	8.19E+00	−1.85E+00
	2.50E−04	−1.11E−03	−9.99E−02	−1.09E+00	8.72E−01	−3.00E−01
	0.00E+00	0.00E+00	0.00E+00	−1.00E+02	0.00E+00	0.00E+00
$j=10$	−2.02E−05	1.96E−04	9.73E−04	−1.01E+02	−2.35E+00	−6.12E−01
	6.00E−05	−3.20E−04	1.60E−04	−1.00E+02	1.61E+00	−6.00E−01
	0.00E+00	0.00E+00	0.00E+00	0.00E+00	−1.00E+02	0.00E+00
$j=11$	−6.85E−05	7.23E−05	1.55E−05	3.83E+00	−1.01E+02	6.38E−01
	1.60E−04	−8.40E−04	−1.00E−04	−9.93E−01	−9.83E+01	−4.30E−01
	0.00E+00	0.00E+00	0.00E+00	0.00E+00	0.00E+00	−1.00E+02
$j=12$	3.70E−04	1.20E−03	1.31E−03	5.90E+00	1.27E−01	−1.04E+02
	1.70E−04	−8.90E−04	−2.40E−04	−4.20E−01	1.66E−01	−1.00E+02
	2.00E−01	0.00E+00	0.00E+00	0.00E+00	0.00E+00	0.00E+00
$j=13$	2.06E−01	−4.27E−04	1.01E−03	−5.32E+00	1.60E+01	−6.19E+00
	2.00E−01	−3.50E−04	−7.00E−05	2.18E+00	1.02E+00	−1.82E+00
	0.00E+00	2.00E−01	0.00E+00	0.00E+00	0.00E+00	0.00E+00
$j=14$	2.98E−03	2.10E−01	3.92E−03	1.29E+01	−1.34E+01	5.45E+00
	6.30E−04	1.99E−01	−6.90E−04	−1.16E+00	−9.57E−01	−1.25E+00
	0.00E+00	0.00E+00	2.00E−01	0.00E+00	0.00E+00	0.00E+00
$j=15$	−4.61E−03	−3.89E−03	2.00E−01	3.55E+00	−1.64E+01	3.70E+00
	4.30E−04	−6.90E−04	2.00E−01	1.40E+00	−9.97E−01	−6.80E−01
	0.00E+00	0.00E+00	0.00E+00	2.00E+02	0.00E+00	0.00E+00
$j=16$	4.05E−05	−3.92E−04	−1.95E−03	2.01E+02	4.69E+00	1.22E+00
	0.00E+00	−5.70E−04	2.80E−04	2.00E+02	1.20E+00	−8.60E−01
	0.00E+00	0.00E+00	0.00E+00	0.00E+00	2.00E+02	0.00E+00
$j=17$	1.37E−04	−1.45E−04	−3.10E−05	−7.65E+00	2.02E+02	−1.28E+00
	2.20E−04	−8.30E−04	−6.30E−04	−8.77E−01	2.02E+02	−4.40E−01
	0.00E+00	0.00E+00	0.00E+00	0.00E+00	0.00E+00	2.00E+02
$j=18$	−7.40E−04	−2.40E−03	−2.61E−03	−1.18E+01	−2.54E−01	2.08E+02
	−1.19E−03	−2.00E−03	−6.80E−04	−2.11E+00	8.96E−01	1.99E+02
	−2.00E−01	0.00E+00	0.00E+00	0.00E+00	0.00E+00	0.00E+00
$j=19$	−2.06E−01	4.27E−04	−1.01E−03	5.32E+00	−1.60E+01	6.19E+00
	−1.99E−01	−9.00E−05	−3.80E−04	3.34E+00	−1.40E+00	−1.58E+00
	0.00E+00	−2.00E−01	0.00E+00	0.00E+00	0.00E+00	0.00E+00

Table 4 (*Continued*)

	θ_x (°)	θ_y (°)	θ_z (°)	δ_x (μm)	δ_y (μm)	δ_z (μm)
j=20	−2.98E−03	−2.10E−01	−3.92E−03	−1.29E+01	1.34E+01	−5.45E+00
	−6.10E−04	−2.00E−01	1.98E−03	−5.41E−01	−8.04E−01	−1.15E+00
	0.00E+00	0.00E+00	−2.00E−01	0.00E+00	0.00E+00	0.00E+00
j=21	4.61E−03	3.89E−03	−2.00E−01	−3.55E+00	1.64E+01	−3.70E+00
	−1.03E−03	−1.56E−03	−1.98E−01	−2.90E−01	1.38E−01	−4.40E−01
	0.00E+00	0.00E+00	0.00E+00	−2.00E+02	0.00E+00	0.00E+00
j=22	−4.05E−05	3.92E−04	1.95E−03	−2.01E+02	−4.69E+00	−1.22E+00
	−5.00E−05	−2.30E−04	1.31E−03	−2.01E+02	1.61E+00	−2.70E−01
	0.00E+00	0.00E+00	0.00E+00	0.00E+00	−2.00E+02	0.00E+00
j=23	−1.37E−04	1.45E−04	3.10E−05	7.65E+00	−2.02E+02	1.28E+00
	2.00E−04	−7.00E−04	−3.00E−05	3.04E−01	−2.00E+02	−1.00E−01
	0.00E+00	0.00E+00	0.00E+00	0.00E+00	0.00E+00	−2.00E+02
j=24	7.40E−04	2.40E−03	2.61E−03	1.18E+01	2.54E−01	−2.08E+02
	1.27E−03	1.05E−03	9.40E−04	6.86E−02	−9.30E−01	−2.01E+02
	1.00E−01	1.00E−01	0.00E+00	0.00E+00	0.00E+00	0.00E+00
j=25	1.04E−01	1.05E−01	2.47E−03	3.78E+00	1.34E+00	−3.70E−01
	1.00E−01	9.91E−02	2.00E−04	−7.90E−01	−6.11E−01	−9.30E−01
	1.00E−01	0.00E+00	1.00E−01	0.00E+00	0.00E+00	0.00E+00
j=26	1.01E−01	−2.16E−03	1.01E−01	−8.87E−01	−1.73E−01	−1.24E+00
	1.00E−01	−2.90E−04	9.99E−02	1.00E+00	1.53E+00	−1.07E+00
	1.00E−01	0.00E+00	0.00E+00	1.00E+02	0.00E+00	0.00E+00
j=27	1.03E−01	−4.10E−04	−4.67E−04	9.80E+01	1.04E+01	−2.48E+00
	1.00E−01	−1.17E−03	−2.40E−04	9.98E+01	1.10E+00	−5.70E−01
	1.00E−01	0.00E+00	0.00E+00	0.00E+00	1.00E+02	0.00E+00
j=28	1.03E−01	−2.86E−04	4.91E−04	−6.49E+00	1.09E+02	−3.73E+00
	1.00E−01	−6.30E−04	0.00E+00	4.53E−01	1.01E+02	−9.10E−01
	1.00E−01	0.00E+00	0.00E+00	0.00E+00	0.00E+00	1.00E+02
j=29	1.02E−01	−1.42E−03	−7.98E−04	−8.57E+00	7.89E+00	1.01E+02
	1.00E−01	−4.70E−04	2.80E−04	1.10E−02	1.22E+00	9.91E+01
	0.00E+00	1.00E−01	1.00E−01	0.00E+00	0.00E+00	0.00E+00
j=30	−8.15E−04	1.03E−01	1.02E−01	8.22E+00	−1.49E+01	4.58E+00
	7.50E−04	9.92E−02	1.00E−01	2.46E−01	8.27E−01	1.10E−01
	0.00E+00	1.00E−01	0.00E+00	1.00E+02	0.00E+00	0.00E+00
j=31	1.51E−03	1.05E−01	9.85E−04	1.07E+02	−4.34E+00	3.34E+00
	−5.00E−05	9.94E−02	2.50E−04	9.88E+01	−7.24E−02	−9.00E−01
	0.00E+00	1.00E−01	0.00E+00	0.00E+00	1.00E+02	0.00E+00
j=32	1.56E−03	1.05E−01	1.94E−03	2.62E+00	9.44E+01	2.09E+00
	2.40E−04	9.97E−02	3.60E−04	−1.08E−02	9.91E+01	−1.20E+00
	0.00E+00	1.00E−01	0.00E+00	0.00E+00	0.00E+00	1.00E+02
j=33	1.12E−03	1.04E−01	6.54E−04	5.44E−01	−6.81E+00	1.07E+02
	1.70E−04	1.00E−01	6.50E−04	−8.00E−01	−2.04E−01	9.88E+01
	0.00E+00	0.00E+00	1.00E−01	1.00E+02	0.00E+00	0.00E+00
j=34	−2.28E−03	−2.14E−03	9.93E−02	1.02E+02	−5.85E+00	2.46E+00
	1.00E−04	−1.12E−03	9.91E−02	9.89E+01	1.25E−01	−5.10E−01
	0.00E+00	0.00E+00	1.00E−01	0.00E+00	1.00E+02	0.00E+00
j=35	−2.24E−03	−2.01E−03	1.00E−01	−2.05E+00	9.29E+01	1.21E+00
	2.70E−04	−1.11E−03	1.00E−01	3.18E−01	1.00E+02	−8.80E−01
	0.00E+00	0.00E+00	1.00E−01	0.00E+00	0.00E+00	1.00E+02
j=36	−2.67E−03	−3.15E−03	9.89E−02	−4.13E+00	−8.32E+00	1.06E+02
	3.70E−04	−8.00E−04	1.01E−01	−2.08E−02	5.46E−01	9.91E+01
	0.00E+00	0.00E+00	0.00E+00	1.00E+02	1.00E+02	0.00E+00
j=37	8.87E−05	−2.68E−04	−9.89E−04	9.68E+01	1.03E+02	−2.65E−02
	1.60E−04	−1.10E−03	−3.00E−04	9.78E+01	1.02E+02	−4.80E−01
	0.00E+00	0.00E+00	0.00E+00	1.00E+02	0.00E+00	1.00E+02
j=38	−3.50E−04	−1.40E−03	−2.28E−03	9.48E+01	2.22E+00	1.05E+02
	9.00E−05	−5.60E−04	−4.90E−04	9.97E+01	1.05E+00	9.88E+01
	0.00E+00	0.00E+00	0.00E+00	0.00E+00	1.00E+02	1.00E+02
j=39	−3.01E−04	−1.27E−03	−1.32E−03	−9.73E+00	1.01E+02	1.04E+02
	6.00E−05	−7.80E−04	3.00E−05	−1.30E−01	1.00E+02	9.96E+01
	−1.00E−01	−1.00E−01	0.00E+00	0.00E+00	0.00E+00	0.00E+00
j=40	−1.04E−01	−1.05E−01	−2.47E−03	−3.78E+00	−1.34E+00	3.70E−01
	−9.95E−02	−1.00E−01	1.00E−05	1.08E+00	1.65E−01	−1.81E+00
	−1.00E−01	0.00E+00	−1.00E−01	0.00E+00	0.00E+00	0.00E+00

Table 4 (*Continued*)

	θ_x (°)	θ_y (°)	θ_z (°)	δ_x (μm)	δ_y (μm)	δ_z (μm)
$j=41$	−1.01E−01	2.16E−03	−1.01E−01	8.87E−01	1.73E−01	1.24E+00
	−9.98E−02	−4.90E−04	−1.00E−01	1.41E+00	7.95E−01	−1.09E+00
	−1.00E−01	0.00E+00	0.00E+00	−1.00E+02	0.00E+00	0.00E+00
$j=42$	−1.03E−01	4.10E−04	4.67E−04	−9.80E+01	−1.04E+01	2.48E+00
	−1.00E−01	5.00E−05	4.00E−05	−9.88E+01	2.32E−01	−1.46E+00
	−1.00E−01	0.00E+00	0.00E+00	0.00E+00	−1.00E+02	0.00E+00
$j=43$	−1.03E−01	2.86E−04	−4.91E−04	6.49E+00	−1.09E+02	3.73E+00
	−9.99E−02	−4.40E−04	1.60E−04	4.18E−01	−1.00E+02	−1.56E+00
	−1.00E−01	0.00E+00	0.00E+00	0.00E+00	0.00E+00	−1.00E+02
$j=44$	−1.02E−01	1.42E−03	7.98E−04	8.57E+00	−7.89E+00	−1.01E+02
	−9.98E−02	−5.10E−04	−5.10E−04	1.24E+00	−8.80E−01	−1.01E+02
	0.00E+00	−1.00E−01	−1.00E−01	0.00E+00	0.00E+00	0.00E+00
$j=45$	8.15E−04	−1.03E−01	−1.02E−01	−8.22E+00	1.49E+01	−4.58E+00
	8.00E−05	−1.00E−01	−1.00E−01	6.62E−01	−1.50E+00	−6.80E−01
	0.00E+00	−1.00E−01	0.00E+00	−1.00E+02	0.00E+00	0.00E+00
$j=46$	−1.51E−03	−1.05E−01	−9.85E−04	−1.07E+02	4.34E+00	−3.34E+00
	3.10E−04	−1.01E−01	2.00E−05	−1.01E+02	7.29E−01	−7.80E−01
	0.00E+00	−1.00E−01	0.00E+00	0.00E+00	−1.00E+02	0.00E+00
$j=47$	−1.56E−03	−1.05E−01	−1.94E−03	−2.62E+00	−9.44E+01	−2.09E+00
	5.20E−04	−1.01E−01	−4.20E−04	−1.76E+00	−9.93E+01	−5.90E−01
	0.00E+00	−1.00E−01	0.00E+00	0.00E+00	0.00E+00	−1.00E+02
$j=48$	−1.12E−03	−1.04E−01	−6.54E−04	−5.44E−01	6.81E+00	−1.07E+02
	4.90E−04	−1.01E−01	−6.40E−04	−1.63E+00	−7.80E−01	−1.00E+02
	0.00E+00	0.00E+00	−1.00E−01	−1.00E+02	0.00E+00	0.00E+00
$j=49$	2.28E−03	2.14E−03	−9.93E−02	−1.02E+02	5.85E+00	−2.46E+00
	1.40E−04	−3.70E−04	−9.89E−02	−1.00E+02	1.26E+00	−9.40E−01
	0.00E+00	0.00E+00	−1.00E−01	0.00E+00	−1.00E+02	0.00E+00
$j=50$	2.24E−03	2.01E−03	−1.00E−01	2.05E+00	−9.29E+01	−1.21E+00
	−1.20E−04	−2.90E−04	−1.00E−01	−3.80E−01	−9.80E+01	−6.40E−01
	0.00E+00	0.00E+00	−1.00E−01	0.00E+00	0.00E+00	−1.00E+02
$j=51$	2.67E−03	3.15E−03	−9.89E−02	4.13E+00	8.32E+00	−1.06E+02
	3.00E−05	−4.30E−04	−1.00E−01	−6.57E−01	6.03E−01	−1.00E+02
	0.00E+00	0.00E+00	0.00E+00	−1.00E+02	−1.00E+02	0.00E+00
$j=52$	−8.87E−05	2.68E−04	9.89E−04	−9.68E+01	−1.03E+02	2.65E−02
	7.00E−05	−3.30E−04	2.30E−04	−9.86E+01	−9.98E+01	−4.30E−01
	0.00E+00	0.00E+00	0.00E+00	−1.00E+02	0.00E+00	−1.00E+02
$j=53$	3.50E−04	1.40E−03	2.28E−03	−9.48E+01	−2.22E+00	−1.05E+02
	8.00E−05	−6.20E−04	8.30E−04	−1.01E+02	1.26E−01	−1.00E+02
	0.00E+00	0.00E+00	0.00E+00	0.00E+00	−1.00E+02	−1.00E+02
$j=54$	3.01E−04	1.27E−03	1.32E−03	9.73E+00	−1.01E+02	−1.04E+02
	4.10E−04	−7.80E−04	4.00E−05	−1.43E+00	−9.87E+01	−1.01E+02

References

[1] Howell LL. Compliant mechanisms. New York, NY: Wiley-Interscience; 2001.

[2] Smith ST. Flexure: element of elastic mechanisms. London, UK: CRC Press LLC; 2000.

[3] Soemers H. Design principles for precision mechanisms. Enschede: T-Pointprint; 2010.

[4] Kang BH, Wen JT, Dagalakis NG, Gorman JJ. Analysis and design of parallel mechanisms with flexure joints. IEEE Transactions on Robotics 2005;21(6):1179–85, http://dx.doi.org/10.1109/TRO.2005.855989.

[5] Yi B, Na H, Chung GB, Kim WK, Suh IH. Design and experiment of a 3 DOF parallel micro-mechanism utilizing flexure hinges. In: IEEE International Conference on Robotics and Automation, 2002. Proceedings. ICRA'02, Vol. 2, IEEE. 2002. p. 1167–72, http://dx.doi.org/10.1109/ROBOT.2002.1014701.

[6] Wu T, Chen J, Chang S. A six-DOF prismatic-spherical-spherical parallel compliant nanopositioner, IEEE Transactions on Ultrasonics. Ferroelectrics and Frequency Control 2008;55(12):2544–51, http://dx.doi.org/10.1109/TUFFC.2008.970.

[7] Liang Q, Zhang D, Song Q, Ge Y. Micromanipulator with integrated force sensor based on compliant parallel mechanism. In: 2010 IEEE International Conference on Robotics and Biomimetics (ROBIO), IEEE. 2010. p. 709–14, http://dx.doi.org/10.1109/ROBIO.2010.5723413.

[8] Dagalakis NG, Albus JS, Wang B-L, Unger J, Lee JD. Stiffness study of a parallel link robot crane for shipbuilding applications. Journal of Offshore Mechanics and Arctic Engineering 1989;111(3):183–93, http://dx.doi.org/10.1115/1.3257146, http://link.aip.org/link/?JOM/111/183/1.

[9] Chen J-S, Hsu W-Y. Design and analysis of a tripod machine tool with an integrated cartesian guiding and metrology mechanism. Precision Engineering 2004;28(1):46–57, http://dx.doi.org/10.1016/S0141-6359(03)00073-4.

[10] Culpepper ML, Anderson G. Design of a low-cost nano-manipulator which utilizes a monolithic, spatial compliant mechanism. Precision Engineering 2004;28(4):469–82, http://dx.doi.org/10.1016/j.precisioneng.2004.02.003.

[11] Chen S-C, Culpepper ML. Design of a six-axis micro-scale nanopositionerhexflex. Precision Engineering 2006;30(3):314–24, http://dx.doi.org/10.1016/j.precisioneng.2005.11.002.

[12] Varadarajan KM, Culpepper ML. A dual-purpose positioner-fixture for precision six-axis positioning and precision fixturing: Part i. modeling and design. Precision Engineering 2007;31(3):276–86, http://dx.doi.org/10.1016/j.precisioneng.2006.11.002.

[13] Varadarajan KM, Culpepper ML. A dual-purpose positioner-fixture for precision six-axis positioning and precision fixturing: part II. characterization and calibration. Precision Engineering 2007;31(3):287–92, http://dx.doi.org/10.1016/j.precisioneng.2006.11.001.

[14] Chao D, Zong G, Liu R, Yu J. A novel kinematic calibration method for a 3DOF flexure-based parallel mechanism. In: 2006 IEEE/RSJ International Conference on Intelligent Robots and Systems, IEEE. 2006. p. 4660–5, http://dx.doi.org/10.1109/IROS.2006.282252.

[15] Yao Q, Dong J, Ferreira P. Design, analysis, fabrication and testing of a parallel-kinematic micropositioning *xy* stage. International Journal of Machine Tools and Manufacture 2007;47(6):946–61, http://dx.doi.org/10.1016/j.ijmachtools.2006.07.007.

[16] Yao Q, Dong J, Ferreira PM. A novel parallel-kinematics mechanisms for integrated, multi-axis nanopositioning: part 1. Kinematics and design for fabrication. Precision Engineering 2008;32(1):7–19, http://dx.doi.org/10.1016/j.precisioneng.2007.03.001.

[17] Brouwer D, de Jong B, Soemers H. Design and modeling of a six dofs mems-based precision manipulator. Precision Engineering 2010;34(2):307–19, http://dx.doi.org/10.1016/j.precisioneng.2009.08.001.

[18] Yang P, Takamura T, Takahashi S, Takamasu K, Sato O, Osawa S, Takatsuji T. Multi-probe scanning system comprising three laser interferometers and one autocollimator for measuring flat bar mirror profile with nanometer accuracy. Precision Engineering 2011;35(4):686–92, http://dx.doi.org/10.1016/j.precisioneng.2011.05.001.

[19] Parker DH, Schwab FR, Shelton JW, Weadon TL. Calibration and modeling of a dual-axis inclinometer. Precision Engineering 2005;29(3):381–5, http://dx.doi.org/10.1016/j.precisioneng.2004.12.001.

[20] McCarthy JM. Geometric design of linkages. New York, NY: Springer-Verlag; 2000.